Graphical Abstract

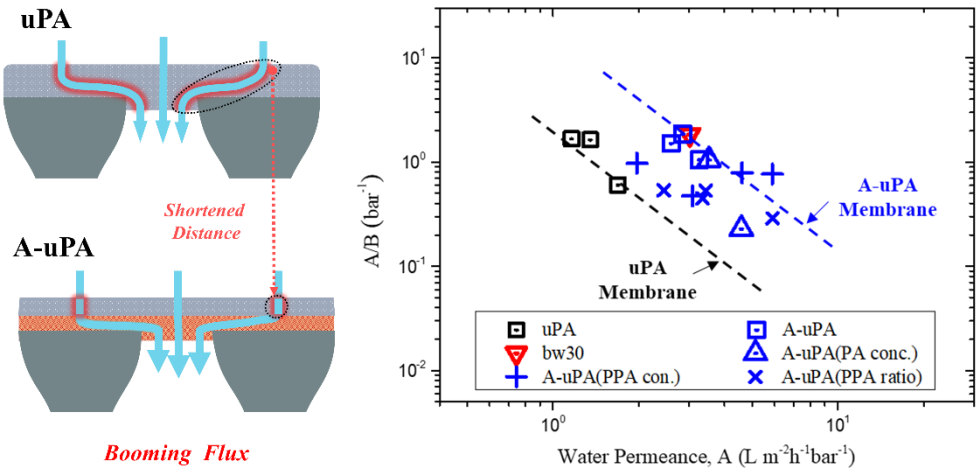

# Ultrathin polyamide nanofilm with an asymmetrical structure: a novel strategy to boost the permeance of reverse osmosis membranes

Bowen Gan[a], Saren Qi[b], Xiaoxiao Song[a*], Zhe Yang[c], Chuyang Y. Tang[c], Xingzhong Cao[d], Yong Zhou[a], Congjie Gao[a]

[a] Centre for Membrane Separation and Water Science & Technology, Ocean College, Zhejiang University of Technology, Hang Zhou, 310014, P. R. China

[b] Suzhou Institute of Nano-Tech and Nano-Bionics (SINANO), Chinese Academy of Sciences, Suzhou 215123, P. R. China

[c] Department of Civil Engineering, the University of Hong Kong, Pokfulam, Hong Kong

[d] Institute of High Energy Physics, CAS, Beijing 100049, China.

*Xiaoxiao Song Tel: +86 (0571) 8832 4135, E-mail address: songxiaoxiao@zjut.edu.cn

## Abstract

Ultrathin polyamide (PA) nanofilm based separation membranes have attracted drastically increasing attention recently. Typically, PA nanofilms with the thickness of around tens of nanometers are supported by a PSF substrate membrane which provides mechanical support. However, the low surface porosity of the PSF substrate membrane has required the transverse diffusion (parallel to the membrane plane) of water molecules in the nanofilm, which causes much longer mean diffusion paths compared to the thickness of the nanofilm. In this study, we address this problem by introducing a much looser polypiperazinamide (PPA) interlayer in between the PA nanofilm and the PSF support membrane, with the PPA nanofilm serving as a low resistance region for water molecules. A dual interfacial polymerization strategy was applied to create an asymmetrical ultrathin polyamide selective layer comprised of a high permeability loose PPA sublayer and a high selectivity dense PA top layer. Quartz crystal microbalance with dissipation (QCMD) techniques and Doppler broadening energy spectroscopy (DBES) were applied to study the asymmetry structure of the ultrathin polyamide nanofilms. Compared with the home-made traditional ultrathin polyamide (uPA) membrane, the asymmetrical ultrathin polyamide (A-uPA) membrane has 2 ~ 2.5 folds higher permeability while maintaining higher salt rejection. Our study demonstrates that the asymmetrical structure can significantly enhance the flux for ultrathin polyamide membranes. Further, the impact of the structure of the top layer and the sublayer on the membrane separation performance was explored by tuning the recipe of the PA top layer and the PPA sublayer.

## 1. Introduction

The selective layer of the conventional polyamide-based desalination membranes is a thin polyamide layer with a typical thickness of a few hundreds of nanometers formed by interfacial polymerization [1-5]. Recently, it has been revealed by high-resolution characterization techniques that the traditional polyamide layers have a large fraction of voids, hence the intrinsic selective layer (typically < 20 nm) is much less than its apparent thickness [6-13]. The voids, connected with the pores on the PSF substrate through a hierarchical pore structure, have been proven to essentially enhance the permeability of the PA layer [2]. Although the surface morphological designs of the polyamide separation layer, such as void fractions [9, 10, 14], wrinkles [15-17], thickness and crosslinking degrees [13, 18-21], have been explored in recent studies to tune the performance of the polyamide layer, relatively fewer researches are focused on studying the intrinsic physicochemical structure of the ultrathin polyamide nanofilm and its impact on the separation properties.

Recently, the researches on developing more efficient ultrathin polyamide nanofilms based membranes have grown drastically. For example, ultrathin polyamide layers with thickness around ten nanometers could be fabricated by electrospray facilitated 3D printing [21, 22], interfacial polymerization at a free interface [18, 23-25], layer-by-layer technology [19, 26], or low-temperature interfacial polymerization [25]. In general, permeability decreases (and salt rejection increases) with the increase of the polyamide thickness as the uniform polyamide chemistry (i.e., the reaction between m-phenylenediamine (MPD) and trimesoyl chloride

(TMC)) in these ultrathin polyamide rejection layers. However, the development of ultrathin membranes faces two major issues: (a) low permeability due to the absence of voids in the PA layer (which act as convection paths for water molecules to reach a pore on the PSF substrate [2, 13, 27-29]) or extra resistance caused by the blockage of substrate pores [30]; (b) the potential low selectivity due to the incompatibility issue between the dense PA structure and porous PSF substrate which causes defects [21].

Here, to address the low permeability and incompatibility issues of the ultrathin PA membranes, we explore the effect of a chemically-bounded polypiperazinamide (PPA) loose interlayer, that is sandwiched between the dense PA layer and the PSF substrate, on the performance of the ultrathin PA membranes. This loose PPA interlayer, formed by the interfacial polymerization between low concentration piperazine (PIP) and TMC, has larger free volumes in its polymer network compared with the MPD/TMC network. This interlayer is expected to act as a gutter layer to facilitate the transport of water molecules and to reduce defect formation. Further, the structure of the asymmetrical ultrathin PA membrane, namely the A-uPA membrane, was analyzed by using Quartz Crystal Microbalance with Dissipation (QCM-D) and Doppler Broadening Energy Spectroscopy (DBES). Then, the impact of the PPA sublayer and PA top layer on the performance of the A-uPA was further explored. This study proposes a new fabrication strategy and forms a theoretical base for constructing higher performance reverse osmosis membranes.

## 2. Materials and Methods

### *2.1. Materials*

Piperazine (PIP, Reagent Plus, 99 %) and m-phenylenediamine (MPD, > 99 %, Aladdin) dissolved in DI water as well as 1,3,5-benzenetricarbonyl trichloride (TMC, > 99 %, Aladdin 98 %,) dissolved in n-hexane (HPLC grade, 97%) were used to fabricate the ultrathin polyamide layers on the PSF ultrafiltration membranes (molecular weight cut-off of 50 KDa, Ande). Sodium chloride (NaCl) and sodium sulfate anhydrous ($Na_2SO_4$) were provided by Xilong Scientific Co. Ltd, which were used in membrane rejection tests. N, N-dimethylformamide (DMF, 99.8 %) was used as a solvent for dissolving the PSF support to prepare isolated PA membranes for characterization. All chemicals were used without any further purification. The BW30 membrane obtained from Dow Filmtech (Minneapolis, MN) was used as a reference for the comparison of membrane performance.

### *2.2. Preparation of uPA and A-uPA membranes*

The uPA membranes were formed by performing the interfacial polymerization techniques on the PSF substrates according to our previous study [19]. A-uPA membranes were formed on the top of the substrates via the multilayer deposition-interfacial polymerization strategy (Figure 1). The formation process of an A-uPA membrane includes two stages. In stage I, a PPA sublayer was fabricated first. For the initial PPA nanofilm deposition, the substrate membrane surface was soaked in a PIP solution with pre-designed low concentrations. Subsequently, excess PIP solution is removed by $N_2$ purging at 2 bar followed with hexane

rinsing. The PIP solution impregnated surface was then reacted with a pre-designed low concentration of TMC dissolved in hexane for 60 s. Finally, removal of excess TMC solution stops the reaction and this results in the formation of a PPA sublayer on the PSF substrate. In stage II, the fabrication methods of top layers dictated the same fabrication route with building the sublayers, except the PIP solution was replaced by the MPD solution. Between the stage I and II, the membrane were dried vertically in a fume hood for 4 mins, during which time the hexane was efficiently drained and dried to avoid pinholes developed in the subsequent stage. After stage II, the membrane was not post-cured to avoid the annealing of the PSF substrate pores and alteration of nanoscale structures of the PA layer, which will cause complexities in the comparison between the uPA and A-uPA membranes. A series of concentration pairs including PIP/TMC and MPD/TMC were examined in this study. For the simplicity, the A-uPA membrane fabricated using PIP/TMC = $x_1/y_1$ and MPD/TMC = $x_2/y_2$ is designated with the name of $x_2/y_2@x_1/y_1$ for short. As the reference to an A-uPA membrane, the corresponding uPA membrane is designated with the name of $x_2/y_2$. After fabrication, all membranes were stored in DI water at 6 °C refrigerator for further use.

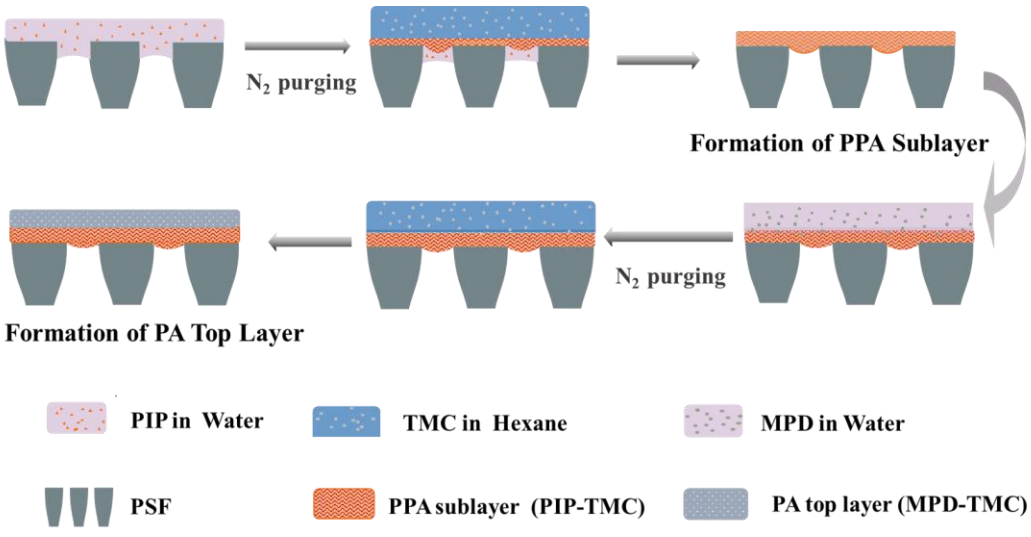

**Figure 1.** The preparation route of the A-uPA membrane.

*2.3. Evaluation of membrane separation performance*

Membrane separation performance (Flux, $J_W$, and Salt Rejection, $R$) was tested with a lab-scale cross-flow RO test setup. The diameter of the membrane chamber was 5 cm and the feed channel depth was 2.5 mm. The cross-flow velocity and pressure were 0.6 L/min and 2.0 MPa, respectively. All membranes were compacted with DI water for 1 hour, then the rejection and flux for NaCl (2000 ppm) and $Mg_2SO_4$ (2000 ppm) were tested for 1 hour. The determination of $J_W$ and $R$ was consistent with our previous study [19]. As a comparison, the performance of the BW30 membrane was also measured with identical conditions.

*2.4. Characterization of the membranes*

The surface and cross-sectional morphologies of membranes were characterized by an ultrahigh-resolution Hitachi 8010U FESEM unit. Cross-sectional images were prepared by fracturing membrane coupons in liquid $N_2$. Before observation, the samples were coated with Pt at standard coating distance (~ 8 cm) with a 15 mA current. Both surface samples and cross-section samples were coated for 45 seconds. The PA nanofilm's topological images and thickness at ambient conditions were obtained using an atomic force microscope (AFM, ICON, Bruker, Billerica, MA) under the tapping mode. Free-standing polyamide (PA) selective layers were isolated by dissolving the substrate PSF layer in pure DMF followed by washing with fresh DMF for 3 cycles of rinsing (3 minutes in each cycle) and soaking (10 minutes in each

cycle). The neat isolated PA layer should be transparent. The free-standing polyamide layer was then transferred onto a silicon wafer for further characterization or analysis.

QCMD characterization

Quartz Crystal Microbalance with Dissipation (QCMD, E4, Q-Sense Biolin Scientific, Sweden) was used to monitor the mass change in the process of interfacial polymerization to form the nanofilms in the A-uPA and uPA membranes. The deposition medium is the cleaned gold sensors (Q-Sense) installed in a QCMD flow chamber cell as previously described [19]. For the deposition of uPA nanofilm, the MPD aqueous solution (0.1 wt %) was first pumped into the chamber. Then, pure n-hexane was pumped in the chamber to remove excess MPD solution. Finally, the TMC/n-hexane solution (0.02 wt %) was pumped through the chamber for the growth of PA nanofilm. The deposition of the A-uPA nanofilm, on the other hand, was accomplished with two stages. In the first stage, the PPA sublayer was formed by the reaction between PIP/water (0.05 wt %) solution and TMC/n-hexane (0.01 wt %) solution following the above-mentioned steps. In the second stage, the PA top layer was formed by the reaction between MPD/water (0.1 wt %) solution and TMC/n-hexane (0.02 wt %) solution directly on the top of the sublayer. Frequency variations were used to quantify the mass change of the sensors induced by the formation of polyamide nanofilm using the Sauerbrey equation in the Q-Tool analysis software (Q-Sense, Biolin Scientific, Sweden) [19].

Doppler Broadening energy spectroscopy (DBES)

158 The variable monoenergy slow positron beam coupled DBES was obtained in the Institute of
159 high energy physics (Beijing, China). The DBES spectrum shows the information about the
160 positron annihilation event and their properties always characterized by the conventional *S* and
161 *W* parameters [31].In this study, The microstructure of membranes was analyzed in terms of
162 the value *S* and *W* parameters and the relation of *W*-*S* with different positron energy. More
163 detailed information regarding the DBES equipment and the definition of *S* and *W* can be found
164 in the references [32, 33]. The mean implantation depth of positron in the polyamide membrane
165 can be calculated by Equation 1 [31, 34]:

166 $$R = (\frac{40}{\rho})E^{1.6} \quad (1)$$

167 Here, the *R* is the mean implantation depth in the membrane. The $\rho$ is the density of materials
168 (polyamide: 1.00~ 1.25 g/cm$^3$ [11, 35-39]). The *E* is the positron energy.

169

170 XPS

171 X-ray photoelectron spectroscopy analysis (XPS, Kratos AXIS Ultra DLD) was used for
172 performing the elemental content of the PA layer within 10 nm of the PA membrane and the
173 radiation source is Al Kα (1486.6eV). For all wide scans and high-resolution scans, a spot area
174 of 700×300μm$^2$ was used. Furthermore, angle-resolved XPS (ARXPS) is used to explore the
175 depth profile of elemental composition in the cross-section of the polyamide selective layer.
176 The analysis depth may be estimated by $d = \lambda \sin\theta$, where *d* is the analysis depth of the overlayer,
177 $\lambda$ is the inelastic mean free path, and $\theta$ is the take-off angle of the analyzed electrons [40, 41].
178 ARXPS measurements for isolated polyamine layers were conducted at four different

179 photoelectron take-off angle with respect to the membrane surface plane (30°, 50°, 70°, and
180 90°), and the corresponding estimated detection depths are 5.0, 7.1, 8.9 and 10.0 nm,
181 respectively [42]. All isolated polyamide nanofilms were transferred onto the gold-coated
182 silicon wafer for further characterization.
183

184 ## 3. Results and discussion

185 *3.1. Characteristics of the uPA and A-uPA membranes*

186 The morphology of the home-made uPA membranes and the A-uPA membranes are
187 characterized by FESEM and the results are shown in Figure 2. On the top surfaces of both
188 membranes, the pores on the PSF substrate are no longer visible in the FESEM images, this
189 suggests the successful formation of the ultrathin polyamide layers. Compared with the PA
190 layer in the conventional RO membrane, both uPA and A-uPA membranes have a smooth
191 surface [2, 19]. Nodules and leaves, which produce a ridge-and-valley structure on the surface
192 of traditional PA membranes, are absent on the surface of both uPA membranes and A-uPA
193 membranes. This agrees well with our previous study [19], in which we discovered that by
194 adopting low concentration pairs of MPD/TMC, a smooth PA layer on top of the polysufone
195 substrate could be formed. This is probably due to the less intense interface polymerization
196 induced less release of $CO_2$ nanobubbles [2, 10, 43]. Note that when MPD concentration was
197 increased from 0.02% to 0.1% (MPD/TMC ratio constantly at 5/1), nodular structures gradually
198 developed at a few locations in both membranes, which are likely a result of the occasional
199 release of $CO_2$ gas nanobubbles [2, 10].

The inserted cross-section FESEM images of the membranes (Figure 2) show the presence of ultrathin PA skin layers in both uPA and A-uPA membranes. However, the accurate measurements of the PA layer thicknesses directly from these images are not reliable due to the lack of clearly defined boundaries between the PA layer and PSU substrate. Hence, the skin layer thicknesses were characterized alternatively using AFM microscopy. For this purpose, the PA skin layers of A-uPA and uPA membranes were isolated and transferred onto a silicon wafer before AFM observation. As shown in Figure 3, a typical height histogram of a uPA skin has two prominent probability peaks, the peak locating near 0 nm marks the height of the silicon wafer baseline, and the sharp peak locating at a higher value represents the height with most probability. Hence, the distance between the two distribution peaks is recognized as the thickness ($\delta$) of the A-uPA and uPA skin layers [18]. As presented in Table 1, the uPA membrane by a series of increasing MPD/TMC concentrations typically has a $\delta$ of 8.2 to 12.3 nm. A similar increasing trend was also reported by Jiang et al. in the free interface formation of ultrathin PA nanofilms [13]. In comparison, the $\delta$ value of the A-uPA membranes fabricated with the 0.05/0.01 PPA sublayer is constantly higher (from 10.64 to 13.00 nm). The constantly higher thickness of the A-uPA skin layers indicates the PPA sublayer contributes to the overall thickness. Nevertheless, in both of the A-uPA and uPA membranes, the nanofilms have thicknesses of ca. one magnitude lower than those reported for conventional PA layers (i.e., a few hundreds of nanometers [13, 44, 45]).

**Table 1**. the surface roughness ($R$) and thickness ($\delta$) of uPA membranes and A-uPA membranes

| Parameter | Top layer MPD concentration (%) | | | | | |
|---|---|---|---|---|---|---|
| | 0.02 | | 0.05 | | 0.1 | |
| | uPA | A-uPA | uPA | A-uPA | uPA | A-uPA |
| $R$[a] | 5.50 | 6.47 | 8.96 | 11.90 | 9.47 | 12.10 |
| $\delta$[b] | 8.21 | 10.64 | 10.50 | 11.02 | 12.30 | 13.00 |

[a.] The concentration ratio of MPD/TMC was kept constantly at 5:1

[b.] The thickness, $\delta$, is defined by the height difference between the two prominent peaks on the height histogram.

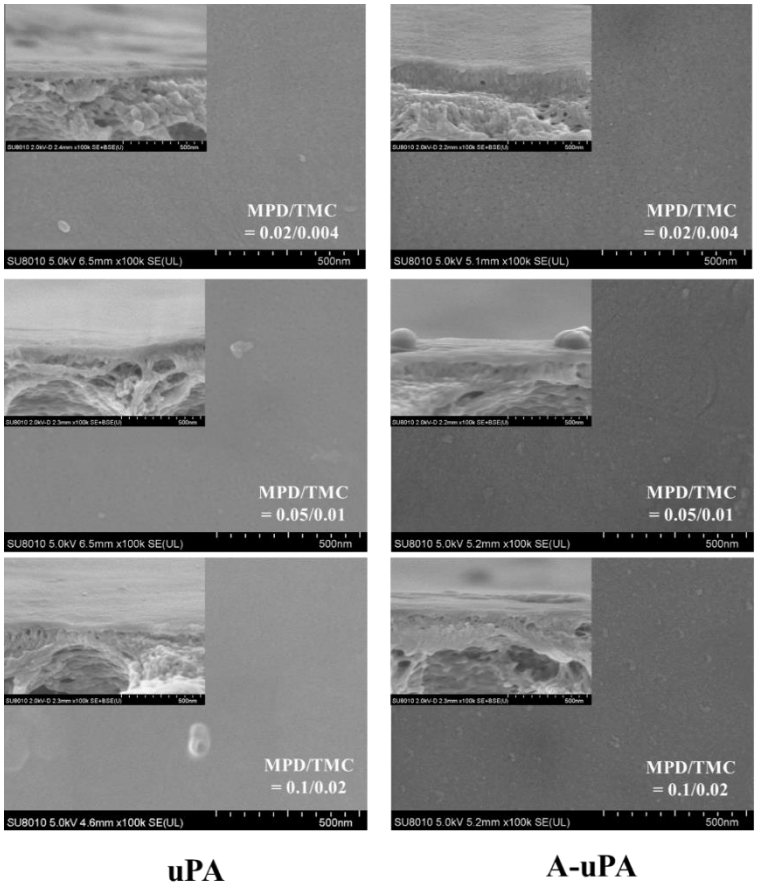


**Figure 2**. FESEM images of the uPA membranes (the left column) and A-uPA membranes (the right column). uPA membranes were fabricated without the PPA sublayer. A-uPA membranes

were fabricated with a PPA sublayer (PIP/TMC = 0.05/0.01). The inserted FESEM image is the corresponding cross-sectional FESEM images to the surface FESEM images.

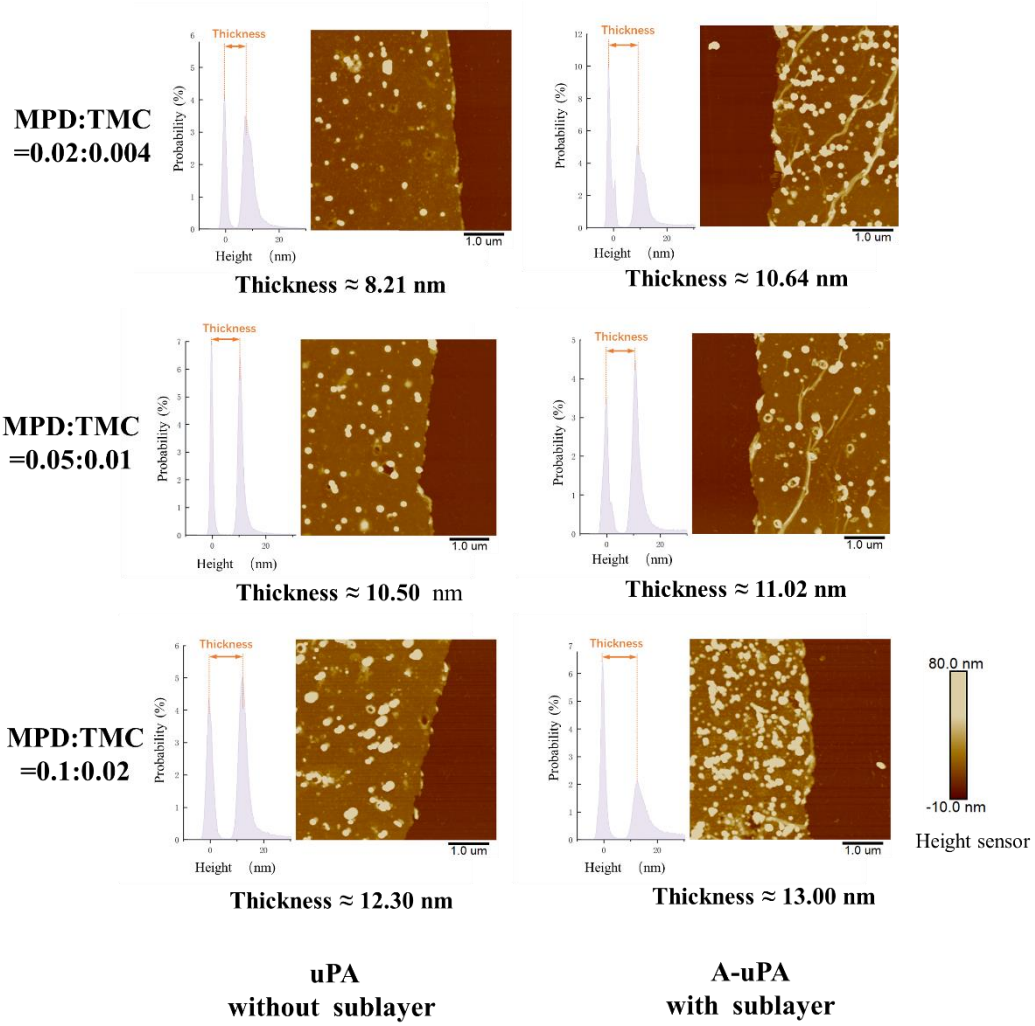


**Figure 3.** AFM images of the uPA and A-uPA nanofilms isolated on the silicon surface ( the left panel shows uPA nanofilms and the right panel shows A-uPA nanofilms (PIP/TMC=0.05/0.01). The diagram to the left of each AFM image is the corresponding height histogram. The color scales for all graphs have been unified.

**Table 2.** Elemental compositions of the A-uPA selective layer (0.05/001@0.05/0.01) measured by XPS

| The XPS results of the top and rear surfaces | Atom percent (%) | | | |
|---|---|---|---|---|
| | O 1s | N 1s | C 1s | O/N |
| Bottom surface | 14.68 | 11.42 | 73.90 | 1.28 |
| Top surface | 16.70 | 11.07 | 72.23 | 1.51 |

To examine the crosslinking degree of the PA network in the A-uPA membrane, the elemental composition of the A-uPA selective layer (0.05/001@0.05/0.01) was characterized by XPS. The results are summarized in Table 2. In theory, for both MPD/TMC and PIP/TMC chemistry, the fully-crosslinked and linearly-crosslinked polyamide network shows an O/N ratio of 1 and 2 respectively [44]. As shown in Table 2 · XPS results suggest that the top and bottom surface of the isolated asymmetrical nanofilm in A-uPA membrane has an O/N ratio of 1.51 and 1.28 respectively, which value is within the range for typical MPD/TMC based RO membranes and PIP/TMC based NF membranes [43, 46, 47]. Note that the XPS penetrates ~ 10 nm for organic samples at a take-off angle of 90°. Therefore, these values reflect the average values of the penetration depth of XPS. As the take-off angle decreases (for ARXPS), the O/N ratio of the top surface showed an increasing trend (Table S1). This phenomenon indicates that the cross-linking degree of the top MPD/TMC layer might be heterogeneous. For example, the O/N ratio of the A-uPA membrane (3.88) even exceeded 2.0 at the take-off angle of 30°, suggesting the presence of abundant oxygen-containing groups on the top surface, which is likely resulted from the hydrolysis of uncrosslinked acyl chloride [48-50]. In conclusion, the XPS results

suggest that the sublayer of PIP/TMC and the top layer of MPD/TMC are successfully formed with a typical cross-linking degree. However, the crosslinking degree of the densest part in the A-uPA nanofilm may be biased by the hydrolysis of TMC at the superficial surface.

### *3.2. The desalination performance of uPA and A-uPA membranes*

#### 3.2.1. The impact of sublayer on the membrane performance

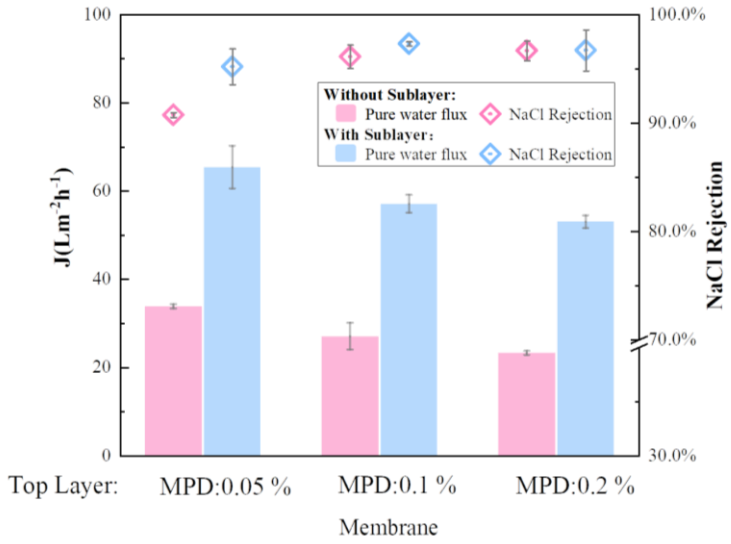


**Figure 4.** The comparison of the desalination performance for the uPA and A-uPA membranes. The sublayers for all membranes were fabricated with PIP/TMC = 0.05/0.01; The top layers for all membranes were fabricated with a fixed concentration ratio of MPD:TMC = 5:1, while the MPD concentration varies. Testing conditions: 2.0 MPa, 2000 ppm NaCl solution.

The desalination performance of the uPA and A-uPA membranes are compared in Figure 4. The A-uPA membranes were fabricated with the same MPD/TMC top layer with the reference uPA membrane, while their sublayers were fabricated with PIP/TMC = 0.05/0.01. For all 3 MPD

concentrations examined, the water flux of the A-uPA membrane increased ~ 2 to 2.5 folds compared with the uPA membrane. Simultaneously, the NaCl rejection of the A-uPA membrane was constantly higher than that of the uPA membrane. For example, the pure water flux for the 0.05/0.01@0.05/0.01 A-uPA membrane was 65.35 L $m^{-2}$ $h^{-1}$, which was approximately 2 folds of that (33.76 L $m^{-2}$ $h^{-1}$) of the uPA membrane. Meanwhile, its NaCl rejection (95.18 %) was higher than the reference (90.73%). The detailed data on membrane performance is listed in Table 3. While the enhancement of salt rejection may be explained by the better compatibility due to the addition of a loose sublayer between the porous UF substrate membrane and the ultrathin PA nanofilm [30], the increment in the water permeability suggests that water molecules encounter less resistance while diffusing through the A-uPA layer. Although not a primary topic to discuss in this study, it should be noted that the salt rejections of both uPA and A-uPA membranes could be further enhanced by tuning the IP time of the MPD/TMC top layer.

**Table 3.** The comparison of desalination performance between the uPA and A-uPA membranes

| MPD conc. (w/v %)[a] | Sublayer[b] | A ($L \cdot m^{-2} \cdot h^{-1} \cdot bar^{-1}$) | Rejection[c] (%) |
|---|---|---|---|
| 0.05 | Without | 1.690 | 90.73% |
| | With | 3.271 | 95.19% |
| 0.1 | Without | 1.351 | 96.11% |
| | With | 2.855 | 97.30% |
| 0.2 | Without | 1.162 | 96.67% |

| | | | |
|---|---|---|---|
| | With | 2.600 | 96.70% |

[a] MPD:TMC ratio was kept constantly at 5 for the top layer fabrication.

[b] The sublayer was fabricated with PIP/TMC = 0.05/0.01.

[c] Testing conditions: 2.0 MPa, 2000 ppm NaCl solution.

3.2.2. The impact of the sublayer recipe on the A-uPA membrane performance

a) b)

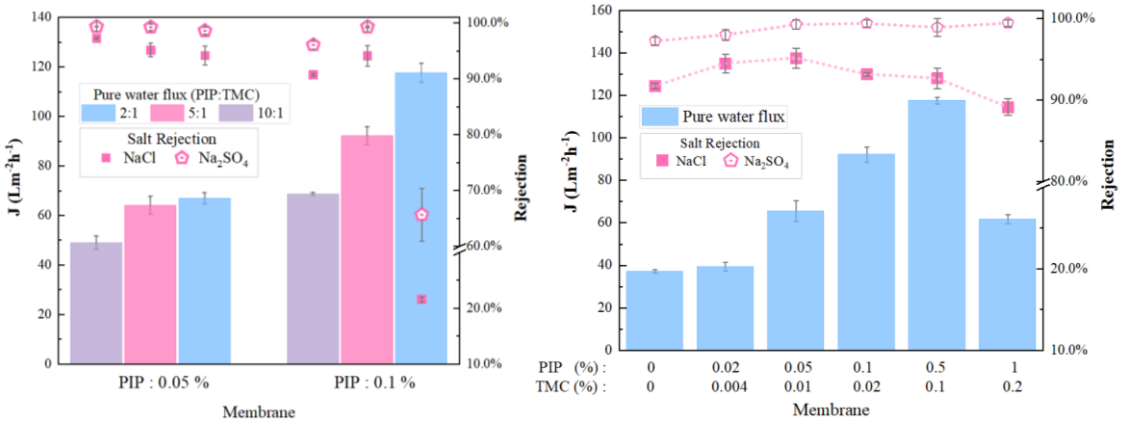


**Figure 5.** (a) NaCl and $Na_2SO_4$ salt rejection and pure water flux for A-uPA membranes with the sublayers fabricated by different PIP:TMC (2, 5, or 10). (b) NaCl and $Na_2SO_4$ salt rejection and corresponding water flux for A-uPA membrane with varied sublayer recipe (0/0; 0.02/0.004; 0.05/0.01; 0.1/0.02; 0.5/0.1; 1/0.2). The top layers for these membranes were fabricated with MPD/TMC = 0.05/0.01. The dotted lines serve as a guide to eye.

To further explore the impact of the sublayer recipe on the A-uPA performance, the PIP:TMC ratio was first tuned while the top layer MPD/TMC recipe was kept constant. As shown in Figure 5, at examined PIP concentrations (0.05 % and 0.1 %), the flux of A-uPA membranes steadily increased as the TMC concentration increased (i.e., decrease of PIP:TMC ratio). In theory, due to the lower diffusion rate of amine molecules in the organic phase, the amine

concentration in aqueous phase should be significantly greater than the TMC concentration organic solution to provide for an optimized reaction stoichiometry [51, 52]. Therefore, as the PIP:TMC ratio decreases, there lacks a proper amount of PIP to produce an as dense PPA network. This theory explains very well the increase in the A-uPA membrane's permeability while TMC concentration increased. Interestingly, the A-uPA membrane series fabricated with high PIP concentration (e.g., 0.1%) generally had higher flux than the corresponding membrane fabricated with low PIP concentration (e.g., 0.05 %). As the higher PIP/TMC concentration tends to form a thicker PPA sublayer [19, 47], one would expect the thicker PPA sublayer resulting in greater resistance. Interestingly, the permeability of the resultant A-uPA membrane increased instead. This phenomenon inspired us to further tune the recipe of the PPA sublayer by adjusting the concentration of the PIP/TMC. The PIP:TMC ratio of 5:1 was chosen in subsequent experiments, as this ratio was able to achieve good NaCl rejection both at 0.05% and 0.1% PIP concentrations.

A series of PIP concentrations in the range of 0.02% to 1% (PIP:TMC = 5) were applied to fabricate the A-uPA membrane. As shown in Figure 5b, the flux of the A-uPA membrane kept increasing to 117.55 L $m^{-2}$ $h^{-1}$ when the PIP concentration was 0.5 %, and then subsequently decreased as the PIP concentration further increased. This is likely caused by the overgrowth of the PPA sublayer at elevated PIP/TMC concentration, therefore the increased hydraulic resistance overrules the incurred benefit from the asymmetrical structure. Meanwhile, the $Na_2SO_4$ rejection kept increasing to 99.47% at 1% PIP concentration, which can be explained

by the enhanced rejection of divalent ions by the PPA sublayer. Interestingly, the maximum NaCl rejection rate appears at a much lower PIP concentration of 0.05 %. At the higher PIP concentrations, the NaCl rejection decreased steadily. The opposite trend of $Na_2SO_4$ and NaCl rejection suggests that while the thicker PPA sublayer fabricated at high PIP/TMC concentration (beyond PIP/TMC=0.05/0.01) promotes the resultant A-uPA's rejection to $Na_2SO_4$, it instead lowers the A-uPA's rejection to NaCl. This phenomenon indicates a less intact PA top layer is formed at a higher PIP/TMC concentration. Possible explanations for this can be (a) highly rough surface (as observed in Figure S2, larger globules appeared at higher PIP/TMC conc.) is not beneficial to the formation of an integral ultrathin top layer; or (b) a thicker PPA layer cause more resistance for MPD diffusion into the organic phase, hence insufficient MPD resulted in less intact PA top layer. Hence, we infer that only a moderately thick sublayer could be beneficial to achieve enhanced permeability while maintaining high NaCl rejection. Besides, to design a proper asymmetrical PA membrane, the sublayer roughness and thickness should be carefully managed to prevent defect formation in the top layer.

### 3.2.3. The impact of the top layer recipe on the A-uPA membrane performance

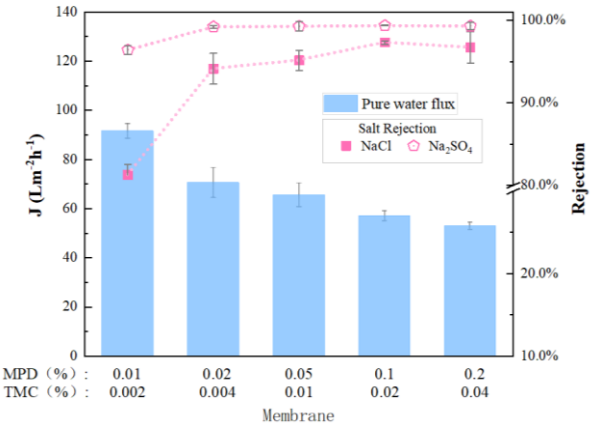

**Figure 6.** NaCl and $Na_2SO_4$ salt rejection and corresponding water flux for A-uPA fabricated with different MPD/TMC concentration in top layer (0.01/0.002, 0.02/0.004, 0.05/0.01, 0.1/0.02, 0.2/0.04). The PPA sublayer was PIP/TMC = 0.05/0.01.

The permeability and selectivity of the A-uPA membrane could be further tuned by altering the recipe of the top layer. As shown in Figure 6, the NaCl rejection of the A-uPA membrane could be further improved to 97.30 % by increasing the MPD concentration to 0.1 %. At the same time, the permeability showed a decreasing trend, demonstrating a typical trade-off relationship with the NaCl rejection [4, 27]. Note that this trend corresponds to the increase of the asymmetrical A-uPA layer thickness (Figure 3). In other words, the increment in the top layer thickness increases the NaCl selectivity although it does not benefit the permeability.

*3.3 The structure of the selective layers of A-uPA membrane*

3.3.1 The QCMD study of the evolution of A-uPA asymmetrical structure

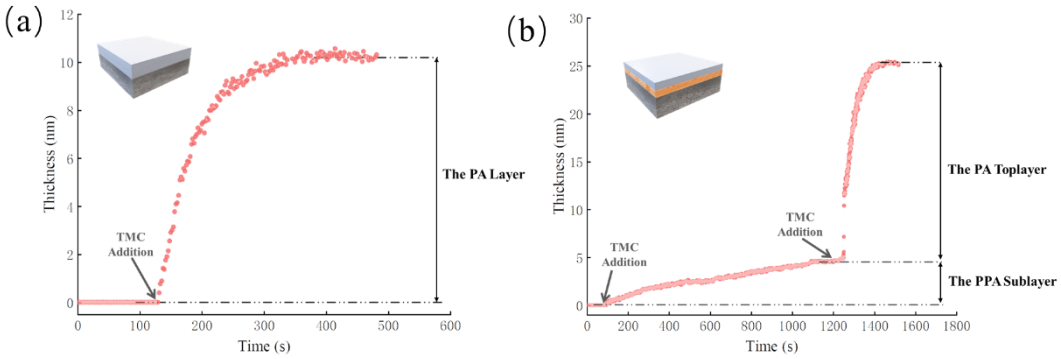


**Figure 7.** QCMD characterization of the evolution process of the selective layers in (a) uPA layer formed with 0.1/0.02 MPD/TMC chemistry; and (b) A-uPA layer formed with a 0.05/0.01

PIP/TMC sublayer and a 0.1/0.02 MPD/TMC top layer.

The QCMD study was performed to study the formation process of the PA layer in the uPA membrane and A-uPA membrane respectively. As shown in Figure 7a, the PA layer in the uPA membrane grew instantaneously upon TMC addition and the thickness gradually increased to 10 nm over the time frame of ca. 120 seconds. The rapidity of the reaction between MPD and TMC has been reported in our previous study [19]. In this work, the final nanofilm formed was ca. 10 nm, which agrees very well with the measurement from the AFM characterization. On the other hand, as shown in Figure 7b, the formation of the A-uPA membrane can be clearly divided into two stages. In stage I, when TMC was added, the sublayer deposited at least an order of magnitude slower than the PA top layer formation (between MPD and TMC), which is probably resulted from the much lower reactivity between PIP/TMC [10]. In stage II, the formation of the top layer went through a similar process with the uPA membrane, demonstrating the successful formation of the top layer. The QCMD characterization provides clear evidence that the A-uPA is composed of a two-layered structure: a sublayer formed by the PIP-TMC chemistry and a top layer formed by the MPD-TMC chemistry. Furthermore, the QCMD result shows that the deposited mass in the top layer is much bigger than the sublayer, which can be explained by the much slower reaction rate between PIP and TMC [30]. Therefore, assuming the density of the MPD/TMC and PIP/TMC are similar (i.e., ca. 1 $g/cm^3$), the MPD/TMC top layer formed should be significantly thicker than the PIP/TMC sublayer.

3.3.2 The DBES study of the A-uPA selective layer

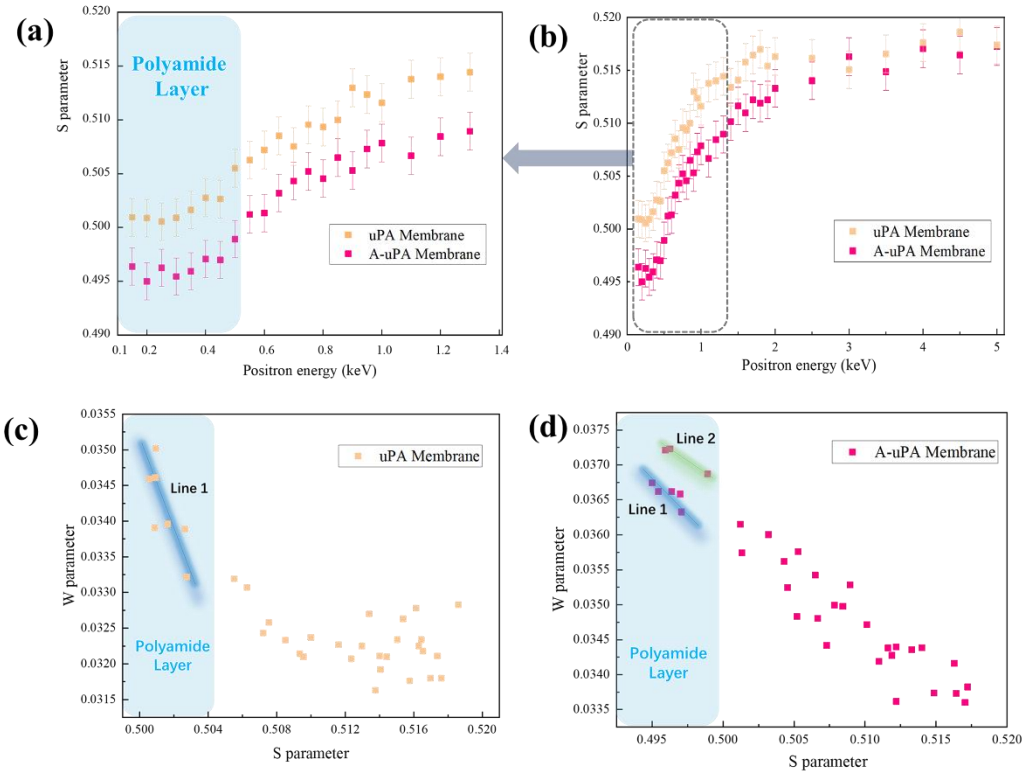


**Figure 8.** (a) the *S* parameter as a function of positron energy for uPA and A-uPA membranes (positron energy 0.1 ~ 1.4 keV); (b) the *S* parameter as a function of positron energy (positron energy 0.15 ~ 5 keV); the *W*-*S* plot in the (c) uPA and (d) A-uPA membranes. In this figure, the uPA membrane was 0.05/001. The A-uPA membrane was 0.05/0.01@0.05/0.01.

To study the free volume in the A-uPA membrane, the DBES experiment was further conducted. The DBES of A-uPA and uPA membranes are compared in Figure 8. The value of *S* parameters is generally related to the free volume in the PA layer [53]. Specifically, The larger *S* value reflects the lager free volume in polyamide layers [14, 54]. The kinetic energy corresponding to the PA nanofilm can be calculated by equation 1 to be around 0.5 KeV, considering the PA

nanofilms of both membranes are ~ 11 nm. As shown in Figures 8a and 8b, the *S* parameter range of the PA nanofilm region (within the region marked in blue) of uPA and A-uPA membrane was ~ 0.500-0.504 and ~ 0.495-0.500, respectively. Hence, within the region of the PA nanofilm, the *S* parameter of the A-uPA membrane was constantly lower than the uPA membrane, which suggests the former has a denser polyamide layer than the latter. This phenomenon can be explained by the formation of a denser top layer in the A-uPA membrane considering the hydrophilic sublayer enhances the absorption of MPD molecules, resulting in a more concentrated MPD solution at the interface [16, 30]. Generally, PA membranes with a looser polyamide structure can favor the increase of water flux at the expense of salt rejection. Interestingly, both of the salt rejection and the pure water flux of A-uPA membranes is higher than uPA membranes as a sub-layer was introduced. In fact, the concurrently increased water flux and salt rejection confirm a key idea in this research that the water permeability of the PA nanofilms can be optimized by designing an asymmetrical polyamide structure without deteriorating the selectivity of the polyamide nanofilm.

On the other hand, the *W* parameter indicates the types of chemical elements or free volume [31, 55, 56]. What's more, the slope of the *W*-*S* relationship curve has been generally adopted as a fingerprint of a specific free volume type [31, 57]. Figures 8c and 8d show the *W*-*S* plot for the uPA membrane and the A-uPA membrane surface respectively. Within the *S* parameter range according to the polyamide nanofilm region, the *W*-*S* plot of the uPA membrane (Figure 8c) shows only one fitted line, which suggests only one type of free volume exists in the PA

412 nanofilm of the uPA membrane. By contrast, the *W-S* plot of the A-uPA membrane shows two
413 fitted lines with different slopes which suggests two types of free volume exist in the polyamide
414 layer of the A-uPA membrane (Figure 8d). The analysis indicates that the A-uPA nanofilms are
415 composed of two distinctive free volumes. Therefore, the DBES analysis is in good agreement
416 with the QCMD study that the asymmetrical structure of the PA nanofilm of the A-uPA
417 membrane comprises of the top and bottom sublayers.
418

419 3.3.3 Discussions on the mechanism for permeance enhancement in the A-uPA membranes

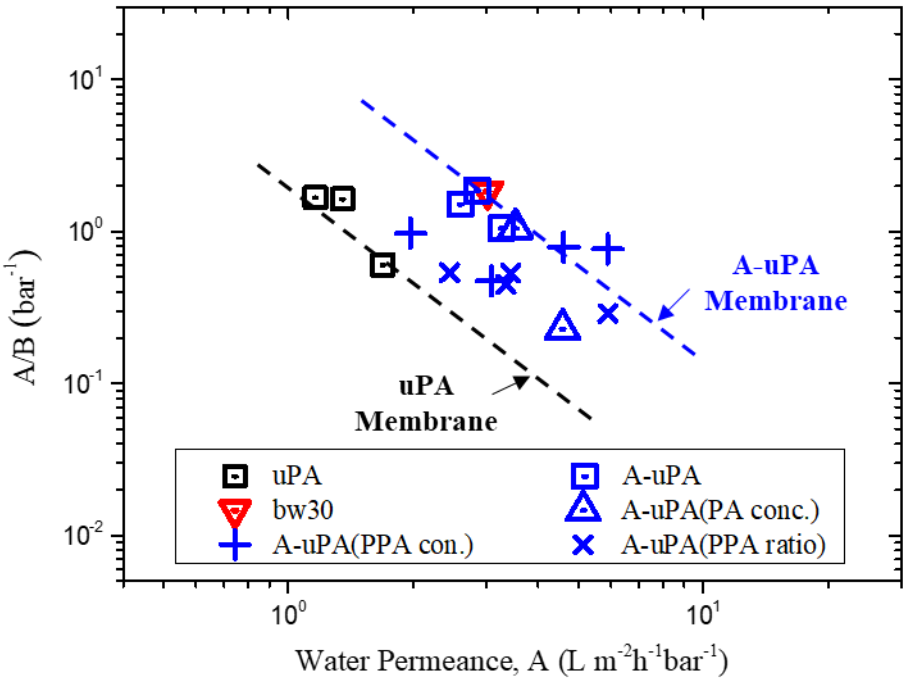


420
421 Figure 9. The permeance-selectivity trade-off relationship for the developed uPA, A-uPA, and
422 the BW30 membrane (reference). uPA and A-uPA refer to the membranes fabricated without
423 and with PPA sublayer respectively (as shown in Figure 4). A-uPA (PA conc.) refer to the A-
424 uPA membranes fabricated using varied PA top layer concentration (Figure 6). A-uPA(PPA
425 conc.) and A-uPA(PPA ratio) refer to the A-uPA membranes fabricated using PPA interlayer
426 varied by the PIP:TMC ratio (Figure 5a) or concentration (Figure 5b), respectively.

Table 4. The performance comparison between a typical A-uPA membrane and the BW30 membrane.

| Membrane types | A ($L \cdot m^{-2} \cdot h^{-1} \cdot bar^{-1}$) | NaCl Rejection ( % ) | A/B ($bar^{-1}$) |
|---|---|---|---|
| A-uPA[a] | 2.86 ± 0.10 | 97.30 ± 0.18 | 1.94 |
| BW30[b] | 3.02 ± 0.08 | 97.15 ± 0.45 | 1.84 |
| BW30[c] | 2.5 ± 0.16 | 95.00 ± 0.50 | 1.97 |

[a] The recipe for the A-uPA membrane was 0.05/0.1@0.1/0.02.

[b] The BW30 membrane was tested in this study with a hydraulic pressure of 2.0 MPa and a CFV of ~ 8 cm/s.

[c] The BW30 membrane was tested in the previous study [19] with a hydraulic pressure of 1.0 MPa and a CFV of ~ 20 cm/s.

The permeance (A) and selectivity (A/B) values of the uPA and A-uPA membranes developed in this study are plotted in Figure 9. It is clearly shown that the permeance-selectivity trade-off line has been upshifted toward the more favorable position after the incorporation of the PPA interlayer (the blue dotted line). Therefore, this supports the core concept of this work: adopting the asymmetrical structure can enhance the permeance of the A-uPA membrane without compromising selectivity. The optimized A-uPA membrane (0.05/0.01@0.1/0.02) achieved slightly better selectivity (A/B) and slightly lower permeance than the BW30 membrane (Table 4). Unlike the rich nanostructures (i.e., nodules and leaves) required for the high permeance of the BW30 membrane [2, 10, 43], the asymmetrical structure of the PA nanofilm in A-uPA represents a new approach for fabrication of high permeance TFC membranes.

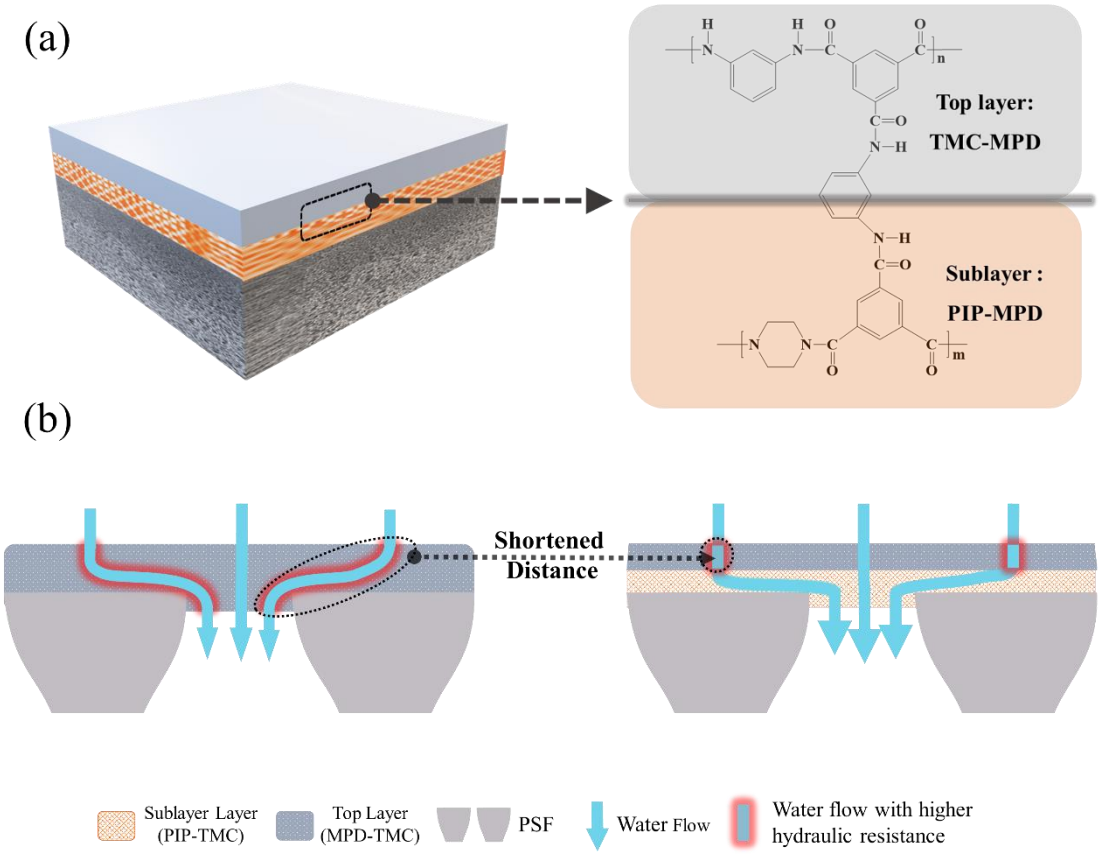


**Figure 10.** (a) the illustration of A-uPA chemical structure based on membrane characterization. (b) the diagram of the water flow in uPA (left) and A-uPA (right). The plain blue arrows represent the water flow through a loose region. The blue arrows with glowing red represent the water flow through a dense region with higher hydraulic resistance.

According to the previous characterization results, the A-uPA chemical structure can be illustrated in Figure 10a. The top layer consists of MPD/TMC and the sublayer consists of PIP/TMC network respectively. As the residual acyl functionalities from the sublayer can continue to react with the amine molecules in the second amine solution [2], this reaction provides for chemical linkages between these two sublayers. In this way, the top layer and sublayer are chemically linked and to form an integral A-uPA selective layer. As shown in

462 Figure S1, the performance of the membranes with only the PPA sublayers indicates the
463 sublayers have very high permeability. For example, when the sublayer formed by the
464 concentration pairs of PIP/TMC = 0.05/0.01, the pure water flux was 529.88 $L$ $m^{-2}$ $h^{-1}$, which
465 corresponds to an $A$ value of ~ 26.5 $L$ $m^{-2}$ $h^{-1}$ $bar^{-1}$. Note this $A$ value is ca. 8 folds of the $A$
466 value of the A-uPA membrane, this suggest that the contribution of the PIP/TMC sublayer to
467 the hydraulic resistance is minor (i.e., ~ 1/8), while the contribution of the MPD/TMC top layer
468 to the hydraulic resistance is major. Simultaneously, the NaCl rejection of the PPA layer is
469 significantly lower than the A-uPA membrane. Considering the much higher water permeance
470 and much lower NaCl rejection of the PPA layer, it is properly addressed as the loose layer.
471
472 Although the attempt to isolate the PIP/TMC layer failed in this study (likely due to its ultrathin
473 nature, the ultrathin layer disintegrated during the dissolution), the mass contribution
474 (estimated from QCMD study) and resistance contribution (from flux measurement) of the PPA
475 layer was ca. 20% and 13%, respectively. The low resistance of the PPA layer is in favor of the
476 permeability increase, however, it hardly explains why the permeability would increase 2 folds.
477 Alternatively, this significant increase may be explained by the "gutter layer" effect that has
478 been similarly employed to decrease interface resistance in gas separation membranes [28, 58].
479 As shown in Figure 6b, when the dense MPD/TMC layer is in direct contact with the PSF
480 substrate, water molecules need to diffuse transversely to get to nano-sized pores on the
481 substrate. The surface porosities of the traditional PSF membranes developed by phase
482 inversion method are typically low (i.e., <10 %) [2]. In this case, the PSF substrate has a surface

pore density of 343 counts/$\mu m^2$ and the most distributed pore sizes between 6 to 13 nm (Figure S3). This translates into a surface porosity between 1.2% and 5.7%. In such circumstance, the average length of a water molecule need to travel to exit from a pore on PSF substrate membrane is much more than the thickness of the PA layer due to the transverse movement (Figure 10b) [29], therefore creating extra resistance within the dense PA top layer. By contrast, when the bottom section of uPA layer is replaced by the PPA sublayer with higher permeability (and much looser structure than the PA layer), the whole hydraulic resistance of selective layer will be directly reduced, as the water molecules diffuse through the dense PA layer to the looser PPA layer which acts as a low-resistance gutter layer to favor molecular transport [28, 58-61]. On the other hand, the PPA gutter layer may prevent the infiltration or growth of dense PA layer into the pore channels of the PSF support during the second stage IP reaction, thus giving rise to the lower PA thickness [30, 47, 62].

## 4. Conclusion

In this study, we have successfully designed and developed an ultrathin polyamide nanofilm with an asymmetrical structure in geometry (i.e., comprising of a dense top layer and loose sublayer) as the selective layer of a PA-based reverse osmosis membrane. Compared with the uPA membrane with a conventional symmetrical structure, the A-uPA allows the pure water flux to increase 2 ~ 2.5 folds while gaining higher salt rejection compared with the uPA membrane. Further, this approach allows for the optimization of the sublayer and top layer of the PA nanofilm separately to tune for better water flux and salt rejection. The asymmetrical

design of PA nanofilm helps to reduce the diffusion resistance induced by the transverse diffusion of water molecules to reach the low-density nanosized pores in PSF support. This is because the mean depth the water molecules need to penetrate within the dense part to reach a looser part in the PA nanofilm is shortened (i.e., the “gutter” layer effect). This study demonstrates for the first time the asymmetric geometry within the polyamide nanofilm can lead to concurrent enhancement of water flux and salt rejection. This provides for a new path for the improved design of conventional desalination membranes. Future work should reveal more specifically how the properties of the interalyer (such as hydrophilicity, porosity, thickness, surface roughness, residual TMC etc) affect the formation and performance of the top layer.

## Acknowledgment

This research was funded by the National Key R&D Program of China (No. 2017YFC0403903), the National Natural Science Foundation of China (No. 21706231), and the Seed Funding for Strategic Interdisciplinary Research Scheme, the University of Hong Kong.

## References

[1] X.Q. Cheng, Z.X. Wang, X. Jiang, T. Li, C.H. Lau, Z. Guo, J. Ma, L. Shao, Towards sustainable ultrafast molecular-separation membranes: From conventional polymers to emerging materials, Prog. Mater Sci., 92 (2018) 258-283.
[2] X. Song, B. Gan, Z. Yang, C.Y. Tang, C. Gao, Confined nanobubbles shape the surface

527 roughness structures of thin film composite polyamide desalination membranes, J. Membr. Sci.,
528 582 (2019) 342-349.
529 [3] F.A. Pacheco, I. Pinnau, M. Reinhard, J.O. Leckie, Characterization of isolated polyamide
530 thin films of RO and NF membranes using novel TEM techniques, J. Membr. Sci., 358 (2010)
531 51-59.
532 [4] Z. Yang, H. Guo, C.Y. Tang, The upper bound of thin-film composite (TFC) polyamide
533 membranes for desalination, J. Membr. Sci., 590 (2019) 117297.
534 [5] C.Y. Tang, Y.-N. Kwon, J.O. Leckie, Effect of membrane chemistry and coating layer on
535 physiochemical properties of thin film composite polyamide RO and NF membranes: II.
536 Membrane physiochemical properties and their dependence on polyamide and coating layers,
537 Desalination, 242 (2009) 168-182.
538 [6] X. Song, J.W. Smith, J. Kim, N.J. Zaluzec, W. Chen, H. An, J.M. Dennison, D.G. Cahill,
539 M.A. Kulzick, Q. Chen, Unraveling the Morphology–Function Relationships of Polyamide
540 Membranes Using Quantitative Electron Tomography, ACS Appl. Mater. Interfaces, 11 (2019)
541 8517-8526.
542 [7] M.M. Kłosowski, C.M. McGilvery, Y. Li, P. Abellan, Q. Ramasse, J.T. Cabral, A.G.
543 Livingston, A.E. Porter, Micro-to nano-scale characterisation of polyamide structures of the
544 SW30HR RO membrane using advanced electron microscopy and stain tracers, J. Membr. Sci.,
545 520 (2016) 465-476.
546 [8] H. Yan, X. Miao, J. Xu, G. Pan, Y. Zhang, Y. Shi, M. Guo, Y. Liu, The porous structure of
547 the fully-aromatic polyamide film in reverse osmosis membranes, J. Membr. Sci., 475 (2015)
548 504-510.
549 [9] L. Lin, R. Lopez, G.Z. Ramon, O. Coronell, Investigating the void structure of the
550 polyamide active layers of thin-film composite membranes, J. Membr. Sci., 497 (2016) 365-
551 376.
552 [10] X.-H. Ma, Z.-K. Yao, Z. Yang, H. Guo, Z.-L. Xu, C.Y. Tang, M. Elimelech, Nanofoaming
553 of polyamide desalination membranes to tune permeability and selectivity, Environ. Sci.
554 Technol. Lett, 5 (2018) 123-130.
555 [11] H.F. Ridgway, J. Orbell, S. Gray, Molecular simulations of polyamide membrane materials
556 used in desalination and water reuse applications: Recent developments and future prospects,
557 J. Membr. Sci., 524 (2017) 436-448.
558 [12] C. Kong, M. Kanezashi, T. Yamomoto, T. Shintani, T. Tsuru, Controlled synthesis of high
559 performance polyamide membrane with thin dense layer for water desalination, J. Membr. Sci.,
560 362 (2010) 76-80.
561 [13] Z. Jiang, S. Karan, A.G. Livingston, Water transport through ultrathin polyamide
562 nanofilms used for reverse osmosis, Adv. Mater., 30 (2018) 1705973.
563 [14] L. Shen, W.-s. Hung, J. Zuo, X. Zhang, J.-Y. Lai, Y. Wang, High-performance thin-film
564 composite polyamide membranes developed with green ultrasound-assisted interfacial
565 polymerization, J. Membr. Sci., 570-571 (2019) 112-119.
566 [15] Z. Tan, S. Chen, X. Peng, L. Zhang, C. Gao, Polyamide membranes with nanoscale Turing
567 structures for water purification, Science, 360 (2018) 518.
568 [16] C. Jiang, L. Tian, Z. Zhai, Y. Shen, W. Dong, M. He, Y. Hou, Q.J. Niu, Thin-film composite

membranes with aqueous template-induced surface nanostructures for enhanced nanofiltration, J. Membr. Sci., 589 (2019) 117244.
[17] Z. Wang, Z. Wang, S. Lin, H. Jin, S. Gao, Y. Zhu, J. Jin, Nanoparticle-templated nanofiltration membranes for ultrahigh performance desalination, Nat. Commun, 9 (2018) 2004.
[18] S. Karan, Z. Jiang, A.G. Livingston, Sub–10 nm polyamide nanofilms with ultrafast solvent transport for molecular separation, Science, 348 (2015) 1347-1351.
[19] X. Song, S. Qi, C.Y. Tang, C. Gao, Ultra-thin, multi-layered polyamide membranes: Synthesis and characterization, Journal of Membrane Science, 540 (2017) 10-18.
[20] X.-H. Ma, Z. Yang, Z.-K. Yao, H. Guo, Z.-L. Xu, C.Y. Tang, Interfacial Polymerization with Electrosprayed Microdroplets: Toward Controllable and Ultrathin Polyamide Membranes, Environ. Sci. Technol. Lett, 5 (2018) 117-122.
[21] M.R. Chowdhury, J. Steffes, B.D. Huey, J.R. McCutcheon, 3D printed polyamide membranes for desalination, Science, 361 (2018) 682.
[22] T. Fujioka, B.E. O'Rourke, K. Michishio, Y. Kobayashi, N. Oshima, H. Kodamatani, T. Shintani, L.D. Nghiem, Transport of small and neutral solutes through reverse osmosis membranes: Role of skin layer conformation of the polyamide film, J. Membr. Sci., 554 (2018) 301-308.
[23] Y. Cui, X.-Y. Liu, T.-S. Chung, Ultrathin Polyamide Membranes Fabricated from Free-Standing Interfacial Polymerization: Synthesis, Modifications, and Post-treatment, Ind. Eng. Chem. Res, 56 (2017) 513-523.
[24] J. Zhu, J. Hou, R. Zhang, S. Yuan, J. Li, M. Tian, P. Wang, Y. Zhang, A. Volodin, B. Van der Bruggen, Rapid water transport through controllable, ultrathin polyamide nanofilms for high-performance nanofiltration, J. Mater. Chem. A, 6 (2018) 15701-15709.
[25] S. Liu, C. Wu, W.-S. Hung, X. Lu, K.-R. Lee, One-step constructed ultrathin Janus polyamide nanofilms with opposite charges for highly efficient nanofiltration, J. Mater. Chem. A, 5 (2017) 22988-22996.
[26] W. Choi, J.-E. Gu, S.-H. Park, S. Kim, J. Bang, K.-Y. Baek, B. Park, J.S. Lee, E.P. Chan, J.-H. Lee, Tailor-Made Polyamide Membranes for Water Desalination, ACS Nano, 9 (2015) 345-355.
[27] H.B. Park, J. Kamcev, L.M. Robeson, M. Elimelech, B.D. Freeman, Maximizing the right stuff: The trade-off between membrane permeability and selectivity, Science, 356 (2017) eaab0530.
[28] M. Kattula, K. Ponnuru, L. Zhu, W. Jia, H. Lin, E.P. Furlani, Designing ultrathin film composite membranes: the impact of a gutter layer, Sci. Rep., 5 (2015) 15016.
[29] G.Z. Ramon, M.C.Y. Wong, E.M.V. Hoek, Transport through composite membrane, part 1: Is there an optimal support membrane?, J. Membr. Sci., 415-416 (2012) 298-305.
[30] Z. Yang, Z.-w. Zhou, H. Guo, Z. Yao, X.-h. Ma, X. Song, S.-P. Feng, C.Y. Tang, Tannic acid/Fe3+ nanoscaffold for interfacial polymerization: Toward enhanced nanofiltration performance, Environ. Sci. Technol., 52 (2018) 9341-9349.
[31] H. Chen, W.-S. Hung, C.-H. Lo, S.-H. Huang, M.-L. Cheng, G. Liu, K.-R. Lee, J.-Y. Lai, Y.-M. Sun, C.-C. Hu, R. Suzuki, T. Ohdaira, N. Oshima, Y.C. Jean, Free-Volume Depth Profile

611 of Polymeric Membranes Studied by Positron Annihilation Spectroscopy: Layer Structure
612 from Interfacial Polymerization, Macromolecules, 40 (2007) 7542-7557.
613 [32] D.W. Gidley, H.-G. Peng, R.S. Vallery, Positron annihilation as a method to characterize
614 porous materials, Annu. Rev. Mater. Res., 36 (2006) 49-79.
615 [33] C. Li, X. Cao, X. Ning, F. Liu, B. Wang, P. Zhang, L. Wei, D. Li, Implantation profiles
616 and depth distribution of slow positron beam simulated by Geant4 toolkit, Phys. Scr., 94 (2019)
617 045301.
618 [34] Y.C. Jean, J.D. Van Horn, W.-S. Hung, K.-R. Lee, Perspective of Positron Annihilation
619 Spectroscopy in Polymers, Macromolecules, 46 (2013) 7133-7145.
620 [35] J.M. Dennison, X. Xie, C.J. Murphy, D.G. Cahill, Density, Elastic Constants, and Thermal
621 Conductivity of Interfacially Polymerized Polyamide Films for Reverse Osmosis Membranes,
622 ACS Appl. Nano Mater., 1 (2018) 5008-5018.
623 [36] T.P. Liyana-Arachchi, J.F. Sturnfield, C.M. Colina, Ultrathin Molecular-Layer-by-Layer
624 Polyamide Membranes: Insights from Atomistic Molecular Simulations, J. Phys. Chem. B, 120
625 (2016) 9484-9494.
626 [37] M. Shen, S. Keten, R.M. Lueptow, Dynamics of water and solute transport in polymeric
627 reverse osmosis membranes via molecular dynamics simulations, J. Membr. Sci., 506 (2016)
628 95-108.
629 [38] T. Yoshioka, K. Kotaka, K. Nakagawa, T. Shintani, H.C. Wu, H. Matsuyama, Y. Fujimura,
630 T. Kawakatsu, Molecular Dynamics Simulation Study of Polyamide Membrane Structures and
631 RO/FO Water Permeation Properties, Membranes (Basel), 8 (2018).
632 [39] N. Zhang, S. Chen, B. Yang, J. Huo, X. Zhang, J. Bao, X. Ruan, G. He, Effect of Hydrogen-
633 Bonding Interaction on the Arrangement and Dynamics of Water Confined in a Polyamide
634 Membrane: A Molecular Dynamics Simulation, J. Phys. Chem. B, 122 (2018) 4719-4728.
635 [40] W.F.S. John F. Moulder, Peter E. Sobol, Handbook of X-ray Photoelectron Spectroscopy:
636 A Reference Book of Standard Spectra for Identification and Interpretation of XPS Data,
637 (1993).
638 [41] N. Suzuki, K.-i. Iimura, S. Satoh, Y. Saito, T. Kato, A. Tanaka, Model for Analysis of XPS
639 Electron Take-off Angle Experiments in Layer-structured Samples: Determination of
640 Attenuation Lengths in a Well-characterized Langmuir–Blodgett Film, Surf. Interface Anal.,
641 25 (1997) 650-659.
642 [42] X. Kong, Z.L. Qiu, C.E. Lin, Y.Z. Song, B.K. Zhu, L.P. Zhu, X.Z. Wei, High
643 permselectivity hyperbranched polyester/polyamide ultrathin films with nanoscale
644 heterogeneity, J. Mater. Chem. A, 5 (2017) 7876-7884.
645 [43] X. Song, B. Gan, S. Qi, H. Guo, C.Y. Tang, Y. Zhou, C. Gao, Intrinsic Nanoscale Structure
646 of Thin Film Composite Polyamide Membranes: Connectivity, Defects, and Structure–
647 Property Correlation, Environ. Sci. Technol., (2020).
648 [44] C.Y. Tang, Y.-N. Kwon, J.O. Leckie, Effect of membrane chemistry and coating layer on
649 physiochemical properties of thin film composite polyamide RO and NF membranes: I. FTIR
650 and XPS characterization of polyamide and coating layer chemistry, Desalination, 242 (2009)
651 149-167.
652 [45] E.M. Vrijenhoek, S. Hong, M. Elimelech, Influence of membrane surface properties on

653 initial rate of colloidal fouling of reverse osmosis and nanofiltration membranes, J. Membr.
654 Sci., 188 (2001) 115-128.
655 [46] O. Coronell, B.J. Mariñas, D.G. Cahill, Depth heterogeneity of fully aromatic polyamide
656 active layers in reverse osmosis and nanofiltration membranes, Environ. Sci. Technol., 45
657 (2011) 4513-4520.
658 [47] S. Karan, Z. Jiang, A.G. Livingston, Sub-10 nm polyamide nanofilms with ultrafast
659 solvent transport for molecular separation, Science, 348 (2015) 1347-1351.
660 [48] C.Y. Tang, Y.-N. Kwon, J.O. Leckie, Probing the nano- and micro-scales of reverse
661 osmosis membranes—A comprehensive characterization of physiochemical properties of
662 uncoated and coated membranes by XPS, TEM, ATR-FTIR, and streaming potential
663 measurements, J. Membr. Sci., 287 (2007) 146-156.
664 [49] V. Freger, Nanoscale Heterogeneity of Polyamide Membranes Formed by Interfacial
665 Polymerization, Langmuir, 19 (2003) 4791-4797.
666 [50] O. Coronell, B.J. Mariñas, X. Zhang, D.G. Cahill, Quantification of Functional Groups
667 and Modeling of Their Ionization Behavior in the Active Layer of FT30 Reverse Osmosis
668 Membrane, Environ. Sci. Technol., 42 (2008) 5260-5266.
669 [51] R.J. Petersen, Composite reverse osmosis and nanofiltration membranes, J. Membr. Sci.,
670 83 (1993) 81-150.
671 [52] V. Freger, Kinetics of film formation by interfacial polycondensation, Langmuir, 21 (2005)
672 1884-1894.
673 [53] Y. He, Y.P. Tang, T.S. Chung, Concurrent Removal of Selenium and Arsenic from Water
674 Using Polyhedral Oligomeric Silsesquioxane (POSS)–Polyamide Thin-Film Nanocomposite
675 Nanofiltration Membranes, Ind. Eng. Chem. Res, 55 (2016) 12929-12938.
676 [54] S. Zhang, K.Y. Wang, T.-S. Chung, H. Chen, Y.C. Jean, G. Amy, Well-constructed
677 cellulose acetate membranes for forward osmosis: Minimized internal concentration
678 polarization with an ultra-thin selective layer, J. Membr. Sci., 360 (2010) 522-535.
679 [55] J.J. Shi, W.Z. Zhao, Y.C. Wu, X.B. Liu, J. Jiang, X.Z. Cao, B.Y. Wang, Evolution of
680 microstructures and hardening property of initial irradiated, post-irradiation annealed and re-
681 irradiated Chinese-type low-Cu reactor pressure vessel steel, J. Nucl. Mater., 523 (2019) 333-
682 341.
683 [56] X.L. Yang, W.X. Zhu, C.D. Wang, H. Fang, T.J. Yu, Z.J. Yang, G.Y. Zhang, X.B. Qin, R.S.
684 Yu, B.Y. Wang, Positron annihilation in (Ga, Mn)N: A study of vacancy-type defects, Appl.
685 Phys. Lett., 94 (2009) 151907.
686 [57] N. Liu, Q. Wang, B. Li, J. Wang, K. Zhang, C. He, L. Wang, L. Song, X. Cao, B. Wang,
687 D. Lin, X. Liu, W. Zhao, Z. Gong, Z. Chen, Point-Defect Distribution and Transformation Near
688 the Surfaces of AlGaN Films Grown by MOCVD, J. Phys. Chem. C, 123 (2019) 8865-8870.
689 [58] K. Xie, Q. Fu, G.G. Qiao, P.A. Webley, Recent progress on fabrication methods of
690 polymeric thin film gas separation membranes for CO2 capture, J. Membr. Sci., 572 (2019) 38-
691 60.
692 [59] Z. Dai, L. Ansaloni, L. Deng, Recent advances in multi-layer composite polymeric
693 membranes for CO2 separation: A review, Green Energy Environ., 1 (2016) 102-128.
694 [60] M. Liu, K. Xie, M.D. Nothling, P.A. Gurr, S.S.L. Tan, Q. Fu, P.A. Webley, G.G. Qiao,

Ultrathin Metal–Organic Framework Nanosheets as a Gutter Layer for Flexible Composite Gas Separation Membranes, ACS Nano, 12 (2018) 11591-11599.
[61] M.J. Yoo, K.H. Kim, J.H. Lee, T.W. Kim, C.W. Chung, Y.H. Cho, H.B. Park, Ultrathin gutter layer for high-performance thin-film composite membranes for CO2 separation, J. Membr. Sci., 566 (2018) 336-345.
[62] S. Gao, Y. Zhu, Y. Gong, Z. Wang, W. Fang, J. Jin, Ultrathin Polyamide Nanofiltration Membrane Fabricated on Brush-Painted Single-Walled Carbon Nanotube Network Support for Ion Sieving, ACS Nano, 13 (2019) 5278-5290.

# Supporting information

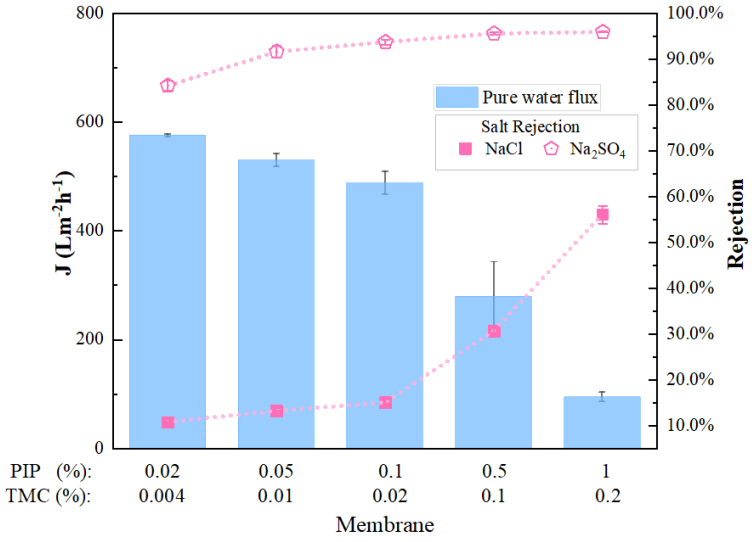


**Figure S1.** The performance of the A-uPA membranes without the top section of the polyamide layers.

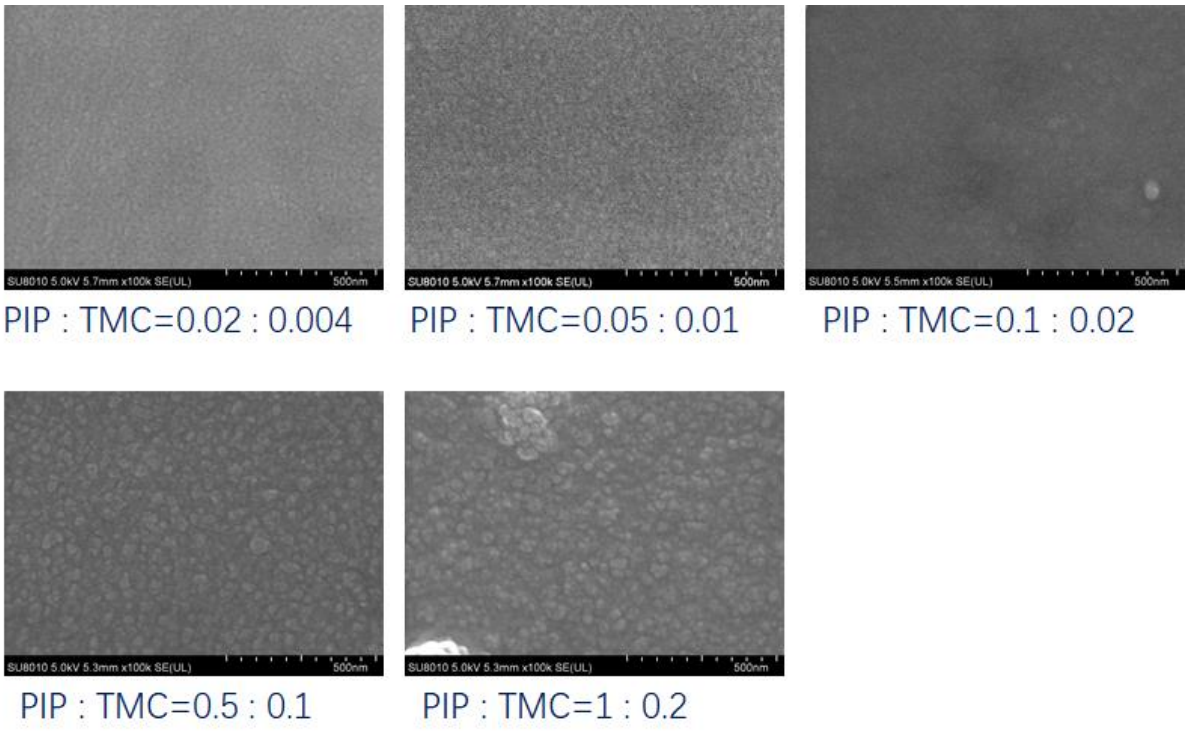


**Figure S2.** The surface of sublayer membranes (PIP-TMC).

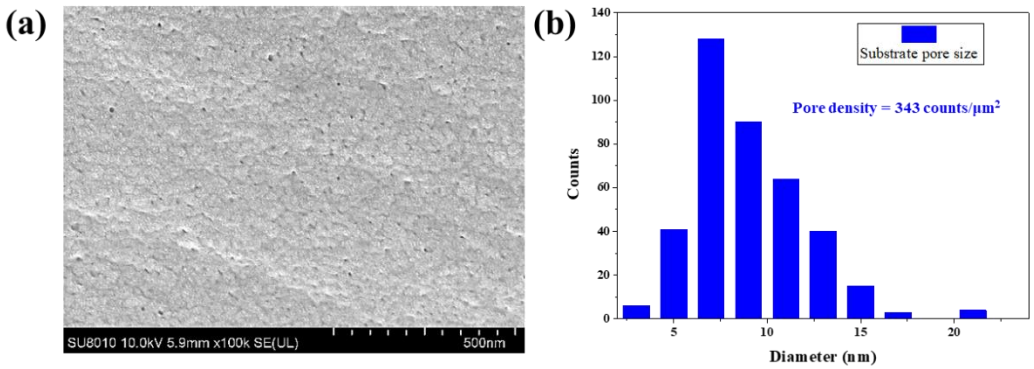


Figure S3. Pore size and density analysis of PSF substrate membrane: (a) The SEM image of the PSF substrate surface. (b) The pore size distribution on the PSF substrate membrane. Pores are counted in the imageJ software.

**Table S1** The result of ARXPS for the A-PA membrane

| The detective angle of ARXPS of the top surface ( Relative Depth ) | Atom percentage (%) | | | |
|---|---|---|---|---|
| | O 1s | N 1s | C 1s | O/N |
| 60° ( 7.1 nm ) | 18.25 | 11.95 | 69.80 | 1.53 |
| 50° ( 8.9 nm ) | 22.59 | 12.76 | 64.65 | 1.77 |
| 30° ( 5 nm ) | 23.93 | 6.16 | 69.91 | 3.88 |

**Declaration of interests**

☒ The authors declare that they have no known competing financial interests or personal relationships that could have appeared to influence the work reported in this paper.

☐ The authors declare the following financial interests/personal relationships which may be considered as potential competing interests:

**Gan Bowen:** Writing- Original draft preparation.

**Saren Qi**: Data curation, Formal Analysis.

**Xiaoxiao Song**: Conceptualization, Methodology, Visualization, Investigation, Vlidation, Writing - Review & Editing, Funding Aquicition.

**Zhe Yang**: Resources, Methodology, Software

**Chuyang Y. Tang**: Resources, Funding Aquicition.

**Xingzhong Cao:** Resources, Methodology.

**Yong Zhou:** Resources, Investigation.

**Congjie Gao:** Supervision, Resources, Funding aquicition